Footprints of Kitaev spin liquid in the Fano lineshape of Raman-active optical phonons

Kexin Feng ◉, Swetlana Swarup ◉, and Natalia B. Perkins◉

School of Physics and Astronomy, University of Minnesota, Minneapolis, Minnesota 55455, USA

We develop a theoretical description of the Raman spectroscopy in the spin-phonon-coupled Kitaev system and show that it can provide observable signatures of fractionalized excitations characteristic of the underlying spin-liquid phase. In particular, we obtain the explicit form of the phonon modes and construct the coupling Hamiltonian based on the D_{3d} symmetry. We then systematically compute the Raman intensity and show that the spin-phonon coupling renormalizes phonon propagators and generates the salient Fano lineshape. We find that the temperature evolution of the Fano lineshape displays two crossovers, and the low-temperature crossover shows pronounced magnetic-field dependence. We thus identify the observable effect of the Majorana fermions and the Z_2 gauge fluxes encoded in the Fano lineshape. Our results are consistent with the phonon Raman scattering experiments in the candidate material α-RuCl$_3$.

Introduction. Raman spectroscopy has proven to be a sensitive experimental probe to study the ground-state properties and the dynamics of various strongly correlated systems [1]. For magnetic insulators, the Raman process couples to the dynamically induced electron-hole pair that connects to the low-energy magnetic states. In magnetically ordered states, the magnetic Raman response shows polarization-dependent peak structure, arising predominantly from one- and two-magnon excitations [2–7]. In the quantum spin liquid (QSL) phase, the Raman spectrum of such low-energy states reveals characteristic low-energy continua, which are fundamentally different from the dispersive collective modes in ordered states. These continua reflect the fractionalization of spins, a hallmark of the QSL [8–16].

Recently, significant efforts were made in the investigation of the QSL state of matter. Mott insulators with strong spin-orbit coupling, e.g., α-RuCl$_3$ [17–28], are promising to realize Kitaev QSL. This QSL is motivated by the famous Kitaev spin model with bond-dependent Ising interactions on a two-dimensional honeycomb lattice [29]. It is exactly solvable with a known gapless QSL ground state. In this model, the spins fractionalize into static Z_2 gauge fluxes and itinerant Majorana fermions amenable to experimental detection.

While various dynamical probes [9,14,30–34] were exploited in several materials to look for signatures of spin fractionalization and their proximity to the Kitaev QSL, employing phonon dynamics and the spin-lattice coupling to detect Kitaev QSL has been less investigated. It was recently suggested that sound attenuation from the phonon decaying into a pair of Majorana fermions [35–37] and the Hall viscosity induced by the time-reversal breaking spin Hamiltonian [36,37] may potentially serve as such a probe. The importance of the spin-phonon coupling in the Kitaev materials is also shown in the interpretation of the thermal Hall transport measurements [38–40].

In this letter, we focus on the Raman spectroscopy of optical phonons, and particularly on the salient Fano lineshape, which arises when the phonon resonance peak couples to the magnetic continuum [41]. This effect is attributed to *spin-dependent* electron polarizability [42,43], which involves a microscopic description of both spin-photon coupling and spin-phonon couplings. The recent work of the authors of Ref. [16] shows that even the simplest form of the couplings can give rise to the Fano line shape. In the experimental studies of the candidate material α-RuCl$_3$ [23–27,44], the pronounced temperature and field dependence of the Fano lineshape indicate rich information about the underlying spin-liquid phase that awaits exploration. However, up to now a clear theoretical description of the Raman scattering in a Kitaev spin-phonon-coupled system is still missing, mainly due to the lack of a proper description of spin-phonon and spin-photon couplings [16].

Here, we make use of the D_{3d} group symmetry of the Kitaev model [45] and propose a theory to describe the Raman scattering of the Kitaev spin-phonon-coupled system. We show that our theory, in which the spin-phonon coupling and spin-photon coupling are explicitly built from the symmetry constraints, quantitatively characterizes the temperature evolution and field dependence of the Fano lineshape of two low-energy optical phonons, observed in the Raman scattering experiments in α-RuCl$_3$ [23–27,44]. These results reveal the clear effects of the Majorana fermions and the Z_2 fluxes, which provide observable signatures for experimental detection of Kitaev QSL.

Model. We consider the spin-phonon Hamiltonian

$$H = H_{\text{s}} + H_{\text{ph}} + H_{\text{s-ph}}. \tag{1}$$

The *first* term is the extended Kitaev honeycomb model [29] $H_{\text{s}} = -J \sum_{\alpha, \mathbf{r} \in A} \sigma_{\mathbf{r}}^{\alpha} \sigma_{\mathbf{r}+\mathbf{M}_{\alpha}}^{\alpha} - \kappa \sum_{\langle \mathbf{r}, \mathbf{r}', \mathbf{r}'' \rangle_{\alpha\gamma}} \sigma_{\mathbf{r}}^{\alpha} \sigma_{\mathbf{r}'}^{\beta} \sigma_{\mathbf{r}''}^{\gamma}$, where $\sigma_{\mathbf{r}}^{\alpha}$ are the Pauli matrices, $\alpha = x, y, z$ and $\mathbf{M}_{\alpha}$ are nearest-
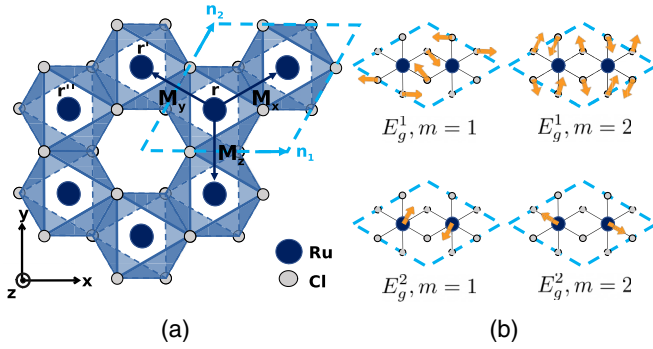
FIG. 1. (a) Crystal structure of α-RuCl$_3$. The unit cell shown in blue-dashed lines is defined by $\mathbf{n_1} = (\sqrt{3}, 0)$ and $\mathbf{n_2} = (\frac{3}{2}, \frac{\sqrt{3}}{2})$ and includes two Ru^{3+} and six Cl$^-$ ions. $\mathbf{M_{x,y}} = (\pm \frac{\sqrt{3}}{2}, \frac{1}{2})$ and $\mathbf{M_z} = (0, -1)$ are nearest-neighbor vectors. The sites $\mathbf{r}$, $\mathbf{r'}$, $\mathbf{r''}$ form a generic three-spin link $\langle \mathbf{r}, \mathbf{r'}, \mathbf{r''} \rangle_{yx}$ as described in the text. (b) Visualization of the eigenmodes of E_g^1 and E_g^2 phonons in xy plane, obtained by linear representation theory (see Sec. A of SM Ref. [49]).

neighbor vectors; J denotes the Kitaev interaction; κ is the strength of the time-reversal symmetry-breaking term, which mimics the effect of an external magnetic field [46]. The three-spin link notation $\langle \mathbf{r}, \mathbf{r'}, \mathbf{r''} \rangle_{\alpha\gamma}$ labels bonds $\mathbf{r r'}$, $\mathbf{r' r''}$ by types α, γ, respectively, and $\beta \neq \alpha, \gamma$. $\mathbf{r}, \mathbf{r'}, \mathbf{r''}$ are counterclockwise ordered adjacent sites [see Fig. 1(a)]. The leading-order term in this Hamiltonian, i.e., the pure Kitaev model, has a symmetry described by the D_{3d} group [47]. The κ term lowers the symmetry to the S_6 group by breaking the two-fold rotation, but we still consider D_{3d} symmetry, which gives the strongest constraint on the theory.

H_s is exactly solvable by the four Majorana fermion representations of spin $\sigma_\mathbf{r}^\alpha = i b_\mathbf{r}^\alpha c_\mathbf{r}$ [29]. In this representation, $H_s = \frac{1}{4} \sum_{\langle \mathbf{rr'} \rangle} h_{\mathbf{rr'}} c_\mathbf{r} c_{\mathbf{r'}}$, where $h_{\mathbf{rr'}} = 2J i\eta_{\mathbf{rr'}} + 2\kappa i\eta_{\mathbf{rr'}} \eta_{\mathbf{r'r''}}$ is the Hamiltonian matrix and $\eta_{\mathbf{rr'}} = i b_\mathbf{r}^\alpha b_{\mathbf{r'}}^\alpha = \pm 1$ is the static Z_2 gauge field on the α-bond, which generates conserved Z_2 fluxes. Within each flux sector, H_s can be further diagonalized to be $H_s = \sum_i \epsilon_i (\beta_i^\dagger \beta_i - 1/2)$, where ϵ_i are the fermionic energy levels and $\beta_i^\dagger$, β_i correspond to the fermionic eigenmodes. Hereafter, the energy and temperature unit will be J unless otherwise specified, which is estimated to be $J \approx 2$ meV $= 23$ K [23,48].

The *second* term in Eq. (1) is the bare phonon Hamiltonian $H_{ph} = H_{ph}(p_i(\mathbf{r}), q_i(\mathbf{r}))$, where $q_i(\mathbf{r}) = (x_1, y_1, z_1, \ldots, x_8, y_8, z_8)_\mathbf{r}$ denotes the displacement field in a unit cell at $\mathbf{r}$, which contains two Ru^{3+} and six Cl$^-$ ions, shown in Fig. 1(a) and S1 in the Supplementary Material (SM) [49]; $p_i(\mathbf{r})$ is the corresponding momentum. Hereafter, we will drop the $\mathbf{r}$ dependence in the phonon fields since the long wavelength of incident light leads to uniform lattice vibrations. By using the D_{3d} of symmetry α-RuCl$_3$, i.e. $[D_{3d}, H_{ph}] = 0$, the eigenmodes of H_{ph} are solved to be the irreducible representations (irreps) of the group, written as linear superpositions of the displacement field (Here, it would be confusing to skip the statement that "the eigenmodes are solved to be the irreducible representation of the groups"): $u_{\Gamma m} = \sum_{i=1}^{24} u_{\Gamma m, i} q_i$. Here, Γ labels the irrep, i.e., $\Gamma = 2A_{1g} + 2A_{2g} + 4E_g + A_{1u} + 3A_{2u} + 4E_u$, among

which the Raman active modes are $\Gamma_R = 2A_{1g} + 4E_g$ [24,50] and m is the dimension of the irrep. (See Sec. A in the SM for a detailed analysis [49]).

In this work, we focus on the two low-energy phonon modes in the Raman spectroscopy [23,24,27]: E_g^1 and E_g^2, whose energies (around 14 meV and 20 meV, respectively) are comparable to the magnetic continuum. They are visualized in Fig. 1(b). The corresponding free phonon Matsubara propagators are written as $\mathcal{D}_{\Gamma m, \Gamma' m'}^{(0)}(i\omega_n) = -\langle T_\tau u_{\Gamma m}(\tau) u_{\Gamma' m'}(0) \rangle_{\omega_n} = \frac{2\omega_\Gamma}{(i\omega_n)^2 - \omega_\Gamma^2} \delta_{\Gamma\Gamma'} \delta_{mm'}$, where ω_Γ is the frequency of the optical phonon and T_τ is the imaginary time ordering operator.

The *third* term in Eq. (1) is the spin-phonon coupling Hamiltonian. It originates from the change of the Kitaev interaction in response to the lattice vibration $J(q_i) = J + \sum_{\Gamma, m} \frac{dJ(q_i)}{du_{\Gamma m}} u_{\Gamma m} + \cdots$, where $\frac{dJ(q_i)}{du_{\Gamma m}}$ is the gradient along the $u_{\Gamma m}$ direction in the manifold of the displacement field. The D_{3d} invariant spin-phonon Hamiltonian is built as

$$H_{\text{s-ph}} = \sum_{\Gamma, m} \lambda_\Gamma \Sigma_{\Gamma m} u_{\Gamma m}, \tag{2}$$

where $\Sigma_{E_g, 1} = \sum_\mathbf{r} (\sigma_\mathbf{r}^x \sigma_{\mathbf{r}+\mathbf{M}_x}^x + \sigma_\mathbf{r}^y \sigma_{\mathbf{r}+\mathbf{M}_y}^y - 2\sigma_\mathbf{r}^z \sigma_{\mathbf{r}+\mathbf{M}_z}^z)$ and $\Sigma_{E_g, 2} = \sum_\mathbf{r} (-\sqrt{3}\sigma_\mathbf{r}^x \sigma_{\mathbf{r}+\mathbf{M}_x}^x + \sqrt{3}\sigma_\mathbf{r}^y \sigma_{\mathbf{r}+\mathbf{M}_y}^y)$ are irreducible representations (irreps) of D_{3d}, and λ_Γ are the coupling constants.

As shown by the perturbative calculation in the SM [49], the phonon propagator is renormalized by the spin-phonon coupling. According to Dyson's equation $\hat{\mathcal{D}} = [(\hat{\mathcal{D}}^{(0)})^{-1} - \hat{\Pi}]^{-1}$, where $\hat{\Pi}$ is the polarization bubble defined as

$$\Pi_{\Gamma m, \Gamma' m'} = -\lambda_\Gamma \lambda_{\Gamma'} \langle T_\tau \Sigma_{\Gamma m}(\tau) \Sigma_{\Gamma' m'}(0) \rangle, \tag{3}$$

$\mathcal{D}_{\Gamma m, \Gamma' m'}$ and $\Pi_{\Gamma m, \Gamma' m'}$ are 4×4 matrices, in which the 2×2 off-diagonal blocks correspond to the mixing between E_g^1 and E_g^2 phonon modes. The components of the off-diagonal blocks are negligible since the corresponding phonon peaks in the Raman spectroscopy are well separated [24].

As will be seen later, the phonon Raman peak parameters, such as the width, center position, and asymmetry factor, are directly related to the real and imaginary parts of the fermionic loop diagrams contained in $\hat{\Pi}$ whose temperature dependence at various values of κ is shown in Fig. S4 of the SM [49]. When temperature increases, both Re $\hat{\Pi}$ and Im $\hat{\Pi}$, evaluated at the bare phonon energies, generically display a two-stage decrease, which is characterized by two crossover temperatures. We can thus expect that this stage-wise temperature dependence in $\hat{\Pi}$ should be reflected in the temperature dependence of the phonon peak parameters, as will be shown next.

Raman response. The Raman scattering of the spin-phonon coupled Kitaev system (1) is described by the Raman operator $\mathcal{R} = \sum_{\mu\mu'} (\mathcal{R}_{\text{em-ph}}^{\mu\mu'} + \mathcal{R}_{\text{em-s}}^{\mu\mu'}) E_{\text{in}}^\mu E_{\text{out}}^{\mu'}$, where E_{in}^μ, $E_{\text{out}}^{\mu'}$ are the electromagnetic fields of the incoming and outgoing light. The second-rank symmetric tensors $\mathcal{R}_{\text{em-ph}}^{\mu\mu'}$ and $\mathcal{R}_{\text{em-s}}^{\mu\mu'}$ microscopically describe the polarizability change of the electronic medium in response to the excitations of phonons and spins [51]. Under the D_{3d} symmetry constraint on the Raman oper-

ator, $\mathcal{R}^{\mu\mu'}_{\text{em-ph}}$ is given by

$$\mathcal{R}^{\mu\mu'}_{\text{em-ph}} = \sum_{\Gamma,m} \mu_\Gamma R^{\mu\mu'}_{\Gamma m} u_{\Gamma m}, \qquad (4)$$

where $R_{\Gamma m}$ are the Raman tensors taken from the irreps of D_{3d}, which are specified as

$$R_{E_g,1} = \begin{bmatrix} c & 0 & d \\ 0 & -c & 0 \\ d & 0 & 0 \end{bmatrix}, \ R_{E_g,2} = \begin{bmatrix} 0 & -c & 0 \\ -c & 0 & d \\ 0 & d & 0 \end{bmatrix}. \quad (5)$$

We take $c = 1$, $d = 0$ in the following computation. μ_Γ are the photon-phonon coupling constants. The coupling of light to spins microscopically originates from its coupling to electric dipoles, which appears as a Wilson line operator that mediates the electronic hopping between the neighboring ions [7,8]. Applying the Loudon-Fleury (LF) approximation [2,3], the magnetic part of the Raman operator can be written as [52]

$$\mathcal{R}^{\mu\mu'}_{\text{em-s}} = \nu \sum_{\alpha, \mathbf{r} \in A} \mathbf{M}^\mu_\alpha \mathbf{M}^{\mu'}_\alpha \sigma^\alpha_{\mathbf{r}} \sigma^\alpha_{\mathbf{r}+\mathbf{M}_\alpha}, \qquad (6)$$

where ν is the photon-spin coupling constant. $\mathcal{R}^{\mu\mu'}_{\text{em-s}}$ also satisfies the symmetry constraint, which can be seen by decomposing it into the irreps of D_{3d} as $\mathcal{R}^{\mu\mu'}_{\text{em-s}} = \nu \sum_m R^{\mu\mu'}_{E_g,m} \Sigma_{E_g,m}$ (details in Sec. B of the SM [49]).

In the *spin-phonon-coupled system*, the Raman intensity is expressed in the interaction picture as $I(\Omega) = \int dt \, e^{i\Omega t} \langle T_t \mathcal{R}(t) \mathcal{R}(0) e^{-i \int dt' H_{\text{s-ph}}(t')} \rangle$, where $\langle \cdots \rangle = \text{Tr}[e^{-\beta H_0} \cdots]/\text{Tr}[e^{-\beta H_0}]$ denotes the statistical average over the Hilbert space of the spin-phonon Hamiltonian $H_0 = H_s + H_{\text{ph}}$, $\beta = 1/T$ is the inverse temperature, and Ω refers to the inelastic energy transfer by the photon. Treating $H_{\text{s-ph}}$ as a perturbation, we perform systematic evaluation of the S-matrix expansion (see Sec. C of the SM [49] for an explicit derivation) and obtain the Matsubara Raman correlated function

$$\mathcal{I}(\tau) = \mathcal{I}_{\text{em-s}}(\tau) + R'_L(\tau) \cdot \hat{\mathcal{D}}(\tau) \cdot R'_R(\tau). \qquad (7)$$

Here, the dot product is on the contraction of (Γ, m) indices, $R'^{\mu\mu'}_{\Gamma m, L(R)}(\tau) = \mu_\Gamma R^{\mu\mu'}_{\Gamma m} + \mathcal{P}^{\mu\mu'}_{\Gamma m, L(R)}(\tau)$ are the renormalized left and right phonon Raman vertices, which consist of the *bare* phonon Raman vertex $\mu_\Gamma R^{\mu\mu'}_{\Gamma m}$ and the *spin-dependent* phonon Raman vertex $\mathcal{P}^{\mu\mu'}_{\Gamma m, L(R)}(\tau)$ [42,43]. The bare phonon Raman vertex generates the phonon peak and constitutes the dominant contribution, while the spin-dependent phonon Raman vertex generates the salient Fano lineshape. $\mathcal{I}^{\mu\mu'}_{\text{em-s}}(\tau) = -\langle T_\tau \mathcal{R}^{\mu\mu'}_{\text{em-s}}(\tau) \mathcal{R}^{\mu\mu'}_{\text{em-s}}(0) \rangle$ contributes to the magnetic continuum in the Raman spectrum. The physical Raman intensity is then obtained by the analytic continuation in the frequency domain $i\Omega_n \to \Omega + i\delta_{\text{ph}}$ followed by the application of the fluctuation-dissipation theorem.

Numerical results. With the developed formalism at hand, we now study the temperature evolution of the Raman spectrum and its κ dependence with the focus on the Fano lineshape. The thermodynamic average of the Raman correlation function over different flux configurations is computed numerically by using the stratified Monte Carlo (strMC) method [37] on a lattice size of $N_1 = N_2 = 25$. We will focus
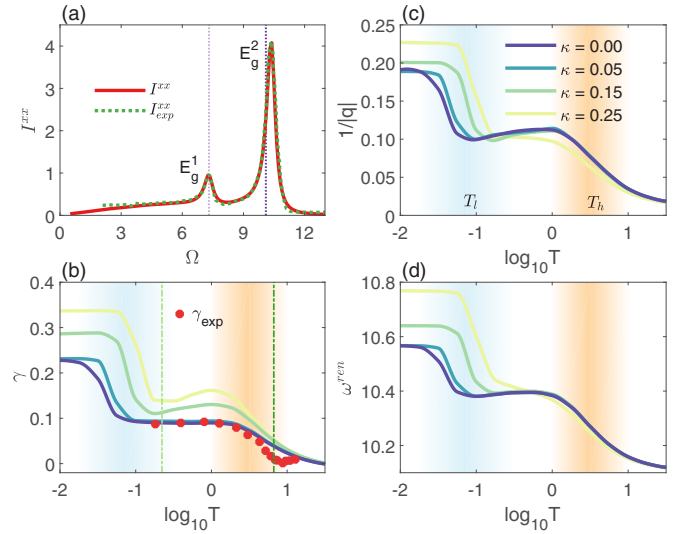

FIG. 2. (a) I^{xx} and I^{xx}_{exp} are, respectively, the strMC-simulated Raman intensity and the experimental intensity from Ref. [23] at $T = 0.22$ and $\kappa = 0$. By fitting I^{xx} to the experimental intensity I^{xx}_{exp}, the best-fit model parameters are obtained as follows: $\omega_\Gamma = [7.31, 10.10]$, $\lambda_\Gamma = [0.25, 0.52]$, $\mu_\Gamma = [0.38, 1.00]$, $\nu = -0.63$. (b)–(d) The temperature dependence of the E^2_g peak curve parameters obtained from the asymmetric Lorentzian fitting: $1/|q|$, γ and ω^{ren}. T_l and T_h are two crossover temperatures. In panel (b), the computed γ was offset by a background line width obtained at $T = 10^{1.5}$. This background line width mainly originates from the artificial broadening δ_{ph} as shown in Sec. D of SM [49]. The red dots are experimental line width γ_{exp}, obtained from Ref. [23]. The two green vertical dashed lines in panel (e) indicate $T = 5$ K and 150 K. The unit conversion we use here is $J \approx 23$ K.

on the xx-scattering geometry to compare with the experiment, and assume $\delta_{\text{ph}} = 0.15$.

To begin with, as shown in Fig. 2(a), we first fit the computed Raman intensity $I^{xx}(\Omega)$ to the experimental Raman intensity $I^{xx}_{\text{exp}}(\Omega)$ obtained from Ref. [23], by tuning the adjustable *model parameters* $\{\omega_\Gamma, \lambda_\Gamma, \mu_\Gamma, \nu\}$ whose best-fit values are written in the caption of Fig. 2. $I^{xx}(\Omega)$ is obtained by using Eq. (7) and evaluated at $T = 0.22$ and $\kappa = 0$. The details of the fitting procedure and justification of the uniqueness of the fitting parameters, after eliminating the overall scaling degree of freedom by setting $\mu_{E^2_g} = 1$, are described in Sec. E of the SM [49]. Remarkably, the best-fit parameter $\lambda_{E^2_g} = 0.52$ yields an estimation of the spin-phonon coupling to be $0.52 \times \sqrt{6} = 1.3J$, [with $\sqrt{6}$ being the norm of the bilinear $\Sigma_{\Gamma m}$ in Eq. (2)], comparable to the first-principle's calculation of magnetoelastic coupling $\approx 4J$ given in Ref. [54].

Next, with the fixed model parameters obtained above, we compute the evolution of the phonon Raman response by changing the temperature and the strength of κ. To quantitatively characterize the phonon peaks, we fit them to the asymmetric Lorentzian curve $I(\Omega) = I_0[q\gamma + (\Omega - \omega^{\text{ren}})]^2/[\gamma^2 + (\Omega - \omega^{\text{ren}})^2]$, where $1/q$ is the asymmetry factor, γ is the half width at half maxima (which is referred to as the line width hereafter), ω^{ren} is the renormalized peak position, and I_0 is the peak intensity.

The temperature evolution of the *curve parameters* $\{1/|q|, \gamma, \omega^{\text{ren}}\}$ of the E^2_g peak for various κ is shown in
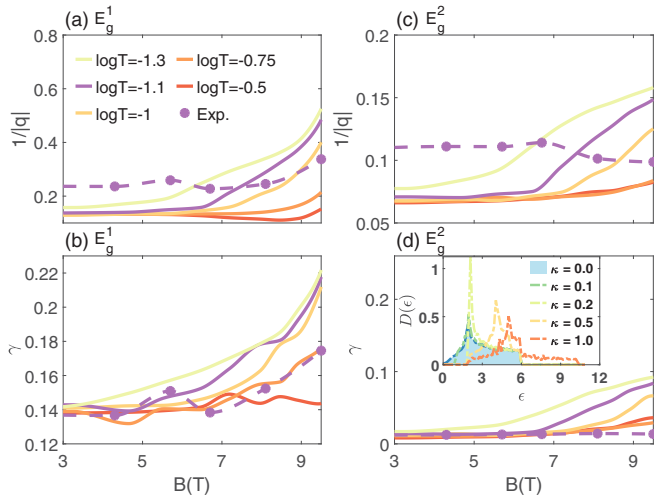
FIG. 3. The magnetic-field dependence of curve parameters $1/|q|$ and γ of two phonon peaks E_g^1 and E_g^2 in the computed Raman spectrum are shown in [(a),(b)] and [(c),(d)], respectively. The purple dots denote experimental data from Ref. [25] measured at $T = 2$ K, i.e., $\log T = -1.1$. The corresponding theoretical curve is also colored purple. The line width γ was offset by the background contribution (see caption of Fig. 2 for the reasoning). The inset of panel (b) shows the density of state of Majorana fermions at various κ [53]. The conversion from κ in the unit of J to magnetic field B in the unit of Tesla follows from [29] $\kappa = \frac{(\mu_B B)^3}{\Delta_{\text{flux}}^2}$, where μ_B is the Bohr magneton and $\Delta_{\text{flux}} = 0.27J$ is the flux energy, and $J \approx 23$ K.

Figs. 2(b) to 2(d). As mentioned above, all curve parameters display a two-stage change with temperature. Two crossover temperatures, namely, T_l (in the blue shaded area) and T_h (in the orange shaded area), correspond, respectively, to the flux proliferation temperature and the major fermionic excitation temperature [37,53,55]. In the T_l region, the curve parameters $\{1/q, \gamma, \omega^{\text{ren}}\}$ decrease significantly, which shows that they are sensitive to the emergent disorder from proliferated Z_2 fluxes. Also, the crossover temperature T_l shows an apparent κ dependence, which reflects the increase of the flux gap energy with κ [53,56]. In the T_h region, the further decrease of the curve parameters is due to the Pauli exclusion principle of fermionic statistics. In Fig. 2(b), we also compare the experimental peak width γ_{exp} obtained in Ref. [23] with the computed γ. Remarkably, in the temperature region between 5 K and 150 K we find a good agreement between them. This result indicates that the source of the anomalous peak width observed in Ref. [23] can indeed be explained by spin-phonon coupling within our theoretical framework. Another noticeable result in Figs. 2(b) to 2(d) is that, at the lowest temperature, the curve parameters become larger with increasing κ. This is because, as the magnetic field increases, more Majorana fermions become energetically comparable with the

phonon modes [see the inset of Fig. 3(d)], and participate in the spin-phonon scattering. So the curve parameters become bigger.

The magnetic-field dependence of $\{1/|q|, \gamma\}$ of E_g^1 and E_g^2 peak for various temperatures in the T_l region is shown in Fig. 3. The conversion from κ to external field B is presented in the caption, where the field direction is assumed to be [111] for simplicity. We can see a clear trend in both peaks that, for a larger temperature in the T_l region, the curve parameters start to increase at a larger magnetic field. This is because the Z_2 flux gap energy is proportional to κ; thus as the temperature becomes larger, the Z_2 fluxes require a higher magnetic field to be gapped out, after which the disorder introduced by Z_2 fluxes becomes weaker and the Fano effects becomes stronger. As a result, the curve parameters start to increase at a larger field.

The computed curve parameters can be compared with the low-temperature experimental from Refs. [25,26]. The data from Ref. [25] is shown in Fig. 3 in the magnetic field region $B = 3 \sim 9T$ containing the putative QSL phase. Remarkably, in Figs. 3(a) and 3(b) there is a discernible increase in the parameters $\{1/|q|, \gamma\}$ in the E_g^1 peak whose magnitude is comparable with the theoretical increase. Our results also suggest that if the increase of the curve parameters at higher temperatures starts at higher fields, then this observation is consistent with the behavior of the Z_2 fluxes. In Figs. 3(c) and 3(d), the experimental field dependence of the E_g^2 peak curve parameters remains featureless. This could be attributed to the fact that the E_g^2 phonon has a higher energy than E_g^1, thus it is less sensitive to the increased population of fermionic modes from the increased field.

Conclusion. We construct a theory to describe the Raman scattering of the spin-phonon-coupled Kitaev system. Based on this theory, we systematically compute the Raman spectrum and explore the temperature evolution and the magnetic field dependence of the phonon peaks in the Raman spectrum, which are consistent with the Raman scattering experiment in α-RuCl$_3$. Our theory clarifies the mechanism of how spin-phonon coupling generates Fano lineshapes and also offers an estimate of the spin-phonon coupling by model fitting. These results open the possibility of experimentally identifying the effects of fractionalized excitations of QSL hidden in the Fano lineshape of phonon Raman peaks.

[1] T. P. Devereaux and R. Hackl, Rev. Mod. Phys. **79**, 175 (2007).

[2] P. Fleury and R. Loudon, Phys. Rev. **166**, 514 (1968).

[3] B. S. Shastry and B. I. Shraiman, Phys. Rev. Lett. **65**, 1068 (1990).

[4] A. V. Chubukov and D. M. Frenkel, Phys. Rev. Lett. **74**, 3057 (1995).

[5] N. Perkins and W. Brenig, Phys. Rev. B **77**, 174412 (2008).

[6] N. B. Perkins, G.-W. Chern, and W. Brenig, Phys. Rev. B **87**, 174423 (2013).

[7] Y. Yang, M. Li, I. Rousochatzakis, and N. B. Perkins, Phys. Rev. B **104**, 144412 (2021).

[8] W.-H. Ko, Z.-X. Liu, T.-K. Ng, and P. A. Lee, Phys. Rev. B **81**, 024414 (2010).

[9] J. Knolle, G.-W. Chern, D. L. Kovrizhin, R. Moessner, and N. B. Perkins, Phys. Rev. Lett. **113**, 187201 (2014).

[10] B. Perreault, J. Knolle, N. B. Perkins, and F. J. Burnell, Phys. Rev. B **92**, 094439 (2015).

[11] B. Perreault, J. Knolle, N. B. Perkins, and F. J. Burnell, Phys. Rev. B **94**, 060408(R) (2016).

[12] B. Perreault, J. Knolle, N. B. Perkins, and F. J. Burnell, Phys. Rev. B **94**, 104427 (2016).

[13] J. Nasu, J. Knolle, D. L. Kovrizhin, Y. Motome, and R. Moessner, Nat. Phys. **12**, 912 (2016).

[14] I. Rousochatzakis, S. Kourtis, J. Knolle, R. Moessner, and N. B. Perkins, Phys. Rev. B **100**, 045117 (2019).

[15] J. Fu, J. G. Rau, M. J. P. Gingras, and N. B. Perkins, Phys. Rev. B **96**, 035136 (2017).

[16] A. Metavitsiadis, W. Natori, J. Knolle, and W. Brenig, arXiv:2103.09828.

[17] K. W. Plumb, J. P. Clancy, L. J. Sandilands, V. V. Shankar, Y. F. Hu, K. S. Burch, H.-Y. Kee, and Y.-J. Kim, Phys. Rev. B **90**, 041112(R) (2014).

[18] J. A. Sears, M. Songvilay, K. W. Plumb, J. P. Clancy, Y. Qiu, Y. Zhao, D. Parshall, and Y.-J. Kim, Phys. Rev. B **91**, 144420 (2015).

[19] A. Banerjee, C. A. Bridges, J.-Q. Yan, A. A. Aczel, L. Li, M. B. Stone, G. E. Granroth, M. D. Lumsden, Y. Yiu, J. Knolle, S. Bhattacharjee, D. L. Kovrizhin, R. Moessner, D. A. Tennant, D. G. Mandrus, and S. E. Nagler, Nat. Mater. **15**, 733 (2016).

[20] A. Banerjee, J. Yan, J. Knolle, C. A. Bridges, M. B. Stone, M. D. Lumsden, D. G. Mandrus, D. A. Tennant, R. Moessner, and S. E. Nagler, Science **356**, 1055 (2017).

[21] A. Banerjee, P. Lampen-Kelley, J. Knolle, C. Balz, A. A. Aczel, B. Winn, Y. Liu, D. Pajerowski, J. Yan, C. A. Bridges, A. T. Savici, B. C. Chakoumakos, M. D. Lumsden, D. A. Tennant, R. Moessner, D. G. Mandrus, and S. E. Nagler, npj Quantum Mater. **3**, 8 (2018).

[22] A. Little, L. Wu, P. Lampen-Kelley, A. Banerjee, S. Patankar, D. Rees, C. A. Bridges, J.-Q. Yan, D. Mandrus, S. E. Nagler, and J. Orenstein, Phys. Rev. Lett. **119**, 227201 (2017).

[23] L. J. Sandilands, Y. Tian, K. W. Plumb, Y.-J. Kim, and K. S. Burch, Phys. Rev. Lett. **114**, 147201 (2015).

[24] G. Li, X. Chen, Y. Gan, F. Li, M. Yan, F. Ye, S. Pei, Y. Zhang, L. Wang, H. Su, J. Dai, Y. Chen, Y. Shi, X.W. Wang, L. Zhang, S. Wang, D. Yu, F. Ye, J.W. Mei, and M. Huang, Phys. Rev. Materials **3**, 023601 (2019).

[25] D. Wulferding, Y. Choi, S.-H. Do, C. H. Lee, P. Lemmens, C. Faugeras, Y. Gallais, and K.-Y. Choi, Nat. Commun. **11**, 1603 (2020).

[26] A. Sahasrabudhe, D. A. S. Kaib, S. Reschke, R. German, T. C. Koethe, J. Buhot, D. Kamenskyi, C. Hickey, P. Becker, V. Tsurkan, A. Loidl, S. H. Do, K. Y. Choi, M. Grüninger, S. M. Winter, Z. Wang, R. Valentí, and P. H. M. van Loosdrecht, Phys. Rev. B **101**, 140410(R) (2020).

[27] D. Lin, K. Ran, H. Zheng, J. Xu, L. Gao, J. Wen, S.-L. Yu, J.-X. Li, and X. Xi, Phys. Rev. B **101**, 045419 (2020).

[28] Y. Wang, G. B. Osterhoudt, Y. Tian, P. Lampen-Kelley, A. Banerjee, T. Goldstein, J. Yan, J. Knolle, H. Ji, R. J. Cava, J. Nasu, Y. Motome, S. E. Nagler, D. Mandrus, and K. S. Burch, npj Quantum Mater. **5**, 14 (2020).

[29] A. Kitaev, Ann. Phys. (NY) **321**, 2 (2006).

[30] J. Knolle, D. L. Kovrizhin, J. T. Chalker, and R. Moessner, Phys. Rev. Lett. **112**, 207203 (2014).

[31] J. Knolle, D. L. Kovrizhin, J. T. Chalker, and R. Moessner, Phys. Rev. B **92**, 115127 (2015).

[32] G. B. Halász, N. B. Perkins, and J. van den Brink, Phys. Rev. Lett. **117**, 127203 (2016).

[33] G. B. Halász, S. Kourtis, J. Knolle, and N. B. Perkins, Phys. Rev. B **99**, 184417 (2019).

[34] Y. Wan and N. P. Armitage, Phys. Rev. Lett. **122**, 257401 (2019).

[35] A. Metavitsiadis and W. Brenig, Phys. Rev. B **101**, 035103 (2020).

[36] M. Ye, R. M. Fernandes, and N. B. Perkins, Phys. Rev. Research **2**, 033180 (2020).

[37] K. Feng, M. Ye, and N. B. Perkins, Phys. Rev. B **103**, 214416 (2021).

[38] Y. Kasahara, T. Ohnishi, Y. Mizukami, O. Tanaka, S. Ma, K. Sugii, N. Kurita, H. Tanaka, J. Nasu, Y. Motome, T. Shibauchi, and Y. Matsuda, Nature (London) **559**, 227 (2018).

[39] M. Ye, G. B. Halász, L. Savary, and L. Balents, Phys. Rev. Lett. **121**, 147201 (2018).

[40] Y. Vinkler-Aviv and A. Rosch, Phys. Rev. X **8**, 031032 (2018).

[41] U. Fano, Phys. Rev. **124**, 1866 (1961).

[42] N. Suzuki and H. Kamimura, J. Phys. Soc. Jpn. **35**, 985 (1973).

[43] T. Moriya, J. Phys. Soc. Jpn. **23**, 490 (1967).

[44] A. Glamazda, P. Lemmens, S.-H. Do, Y. S. Kwon, and K.-Y. Choi, Phys. Rev. B **95**, 174429 (2017).

[45] Y.-Z. You, I. Kimchi, and A. Vishwanath, Phys. Rev. B **86**, 085145 (2012).

[46] While we understand that the minimal model describing describing α-RuCl$_3$ contains other terms [57], here we show that the main features of the observed phonon dynamics can be understood already within the pure Kitaev model.

[47] The sixfold rotation C_6 in the C_{6v} group corresponds to sixfold rotoreflection S_6 in D_{3d} and $S_6 = C_{6v}\sigma_h$, where σ_h is a mirror reflection w.r.t the honeycomb plane [45].

[48] Note that, as our model is written in terms of the Pauli matrices, the coupling constant J here is 1/4 of the coupling for spin-1/2.

[49] See Supplemental Material at http://link.aps.org/supplemental/10.1103/PhysRevB.105.L121108 for more information, which includes Refs. [58–66].

[50] G. Guizzetti, E. Reguzzoni, and I. Pollini, Phys. Lett. A **70**, 34 (1979).

[51] M. S. Dresselhaus, G. Dresselhaus, and A. Jorio, *Group Theory: aApplication to the Physics of Condensed Matter* (Springer Science and Business Media, New York, 2007).

[52] In a recent study [7], some of us showed that in the Kitaev candidate materials non-LF terms also appear in the magnetic Raman scattering. However, their main effects mainly appear at energies below J, so they will not change much physics at the energy scale above J. This is why here we constrain our consideration to the LF approximation.

[53] K. Feng, N. B. Perkins, and F. J. Burnell, Phys. Rev. B **102**, 224402 (2020).

[54] D. A. S. Kaib, S. Biswas, K. Riedl, S. M. Winter, and R. Valentí, Phys. Rev. B **103**, L140402 (2021).

[55] J. Nasu, M. Udagawa, and Y. Motome, Phys. Rev. B **92**, 115122 (2015).

[56] V. Lahtinen, New J. Phys. **13**, 075009 (2011).

[57] S. M. Winter, A. A. Tsirlin, M. Daghofer, J. van den Brink, Y. Singh, P. Gegenwart, and R. Valenti, J. Phys.: Condens. Matter **29**, 493002 (2017).

[58] T. Inui, Y. Tanabe, and Y. Onodera, *Group Theory and its Applications in Physics*, Vol. 78, (Springer Science and Business Media, New York, 1996), Chaps. 4.13.2, 6.2, pp. 78, 106–107.

[59] Equivalent to Schur's Lemma in group representation theory.

[60] D. S. Dummit and R. M. Foote, *Abstract Algebra*, Vol. 3, (Wiley, Hoboken, NJ, 2004).

[61] J.-P. Serre, *Linear Representations of Finite Groups*, Vol. 42, (Springer, New York, 1977), Chap. 2.7, pp. 23–24.

[62] The explicit result was shared by the author through a private communication.

[63] E. Kroumova, M. Aroyo, J. Perez-Mato, A. Kirov, C. Capillas, S. Ivantchev, and H. Wondratschek, Phase Transitions: A Multinational J. **76**, 155 (2003).

[64] Note that here the coordinate system as illustrated in the figure was rotated from the standard settings of space group.

[65] G. D. Mahan, *Many-Particle Physics* (Springer Science and Business Media, New York, 2013).

[66] T. T. Mai, A. McCreary, P. Lampen-Kelley, N. Butch, J. R. Simpson, J.-Q. Yan, S. E. Nagler, D. Mandrus, A. R. Walker, and R. V. Aguilar, Phys. Rev. B **100**, 134419 (2019).